J Elast
DOI 10.1007/s10659-017-9626-5

A Computational Model of the Biochemomechanics of an Evolving Occlusive Thrombus

Manuel K. Rausch[1,2] · **Jay D. Humphrey**[1]

Received: 9 May 2016

Abstract Blood clots are fundamental to preventing excessive blood loss in cases of vascular injury and to promoting subsequent wound healing, but also to many disease conditions. The biomechanical properties of clots play important roles in dictating the natural history in health and disease. In this paper, we present a novel multiscale computational model of biological, chemical, and mechanical contributions to the maturation of an occlusive clot from a fibrin-dominated to a collagen-dominated tissue. For an occlusive venous thrombus, simulations show the potential coupling between mechanical deformations and chemical processes, which can result in competing phenomena. This mixture-based framework also promises to guide future experimentation, which is vitally needed to increase our understanding of the complex and important biochemomechanics of clots.

Keywords Growth and remodeling · Deep vein thrombosis · Microsphere · Venous thrombosis · Multiscale

Mathematics Subject Classification 74F10

1 Introduction

Thrombosis, that is the formation of a blood clot, is essential for controlling hemorrhage in cases of tissue injury. Yet, many devastating disease conditions can also result from a thrombus—heart attack, stroke, and pulmonary embolism to name a few [23, 33, 36].

✉ M.K. Rausch
manuel.rausch@utexas.edu

J.D. Humphrey
jay.humphrey@yale.edu

1 Department of Biomedical Engineering, Yale University, 55 Prospect Street, New Haven, CT 06520, USA

2 Department of Aerospace Engineering & Engineering Mechanics, University of Texas at Austin, 210 E 24th St, Austin, TX 78712, USA

Published online: 08 March 2017

Notwithstanding the critical importance of the biochemistry involved in the formation, lysis, or maturation of a clot, quantification of the evolving biomechanical properties is equally important for understanding the role of thrombus in both physiology and pathophysiology. Whereas many prior biomechanical studies have focused on the initial few minutes of the blood clotting cascade [51, 52], here we introduce a new model within the framework of a reactive/constrained mixture theory that allows studying the possible longer term evolution of a thrombus. Specifically, we are interested in the competition between thrombus degradation or lysis and the deposition of structural constituents during maturation, which may determine whether thrombus embolizes, that is, sheds fragments into the flowing blood, or whether it persists intact [20].

The blood clotting cascade is well studied [15] and can be captured via complex systems of differential equations that describe reactions among the many different biomolecules [17, 34]. However, given that the initial clotting process occurs within minutes and our interest is in longer term maturation of the clot (on the order of weeks), we focus on the latter by prescribing the biomechanical properties of a fresh fibrin network in our initial model. During its evolution, we consider thrombus to be a reactive mixture, consisting of a constrained mixture of two structurally significant solid constituents, ubiquitous interstitial fluid, a generic family of migrating synthetic cells, and one key biomolecule. This biomolecule, plasmin(ogen), which represents both the zymogen plasminogen and its active form, the serine protease plasmin, facilitates the degradation of one of the solid constituents (fibrin) while the cells, ostensibly (myo)fibroblasts, deposit the other solid constituent (collagen fibers). We use the term (myo)fibroblasts for it is the fibroblast that is recruited and then changes phenotypically to increase its production of collagen and better organize the matrix; we do not model the phenotypic modulation however. To further focus our attention on the longer term maturation of a fibrin-based clot into a more collagenous tissue, we assume that local plasmin levels correspond directly to those for plasminogen. For conceptual purposes, we also consider plasmin(ogen) and (myo)fibroblasts as non-charged "solutes" that diffuse and advect within the interstitial fluid that saturates the pores of the solid. Because local deformations affect the transport of important thrombotic and thrombolytic biomolecules, the migration of relevant synthetic cell species, critical reactions between constituents and biomolecules, biological processes such as collagen deposition, our model, for the first time, additionally includes mechanically and directionally sensitive constitutive equations for transport and migration as well as mechanically and directionally sensitive reaction equations [2, 12, 13, 49].

The primary goal of this work is to develop a first framework to model the nonlinear, anisotropic mechanical behavior of evolving thrombus by capturing the roles of specific cells and biomolecules within a multiscale framework that largely melds concepts from Ateshian [6, 7] and Humphrey and Rajagopal [27]. The secondary goal of our work is to use our newly introduced approach to investigate mechanically-mediated feedback mechanisms that may predict different fates of a thrombus, including resolution, maturation, or embolization. This capability may be critical from both clinical and basic scientific standpoints as the location of advanced lysis and/or reduced collagen deposition may determine whether thrombus embolizes partially and fragments or dislodges in whole, thus increasing the risk of a fatal pulmonary embolus for example. For purposes of illustration, our computational model focuses on the evolution of occlusive venous thrombus and is based on data available from a well-accepted mouse model [18, 32]. The basic framework is much more general, however.

2 Modeling Framework

2.1 Solid Constituents—Fibrin and Collagen

The solid portion of an evolving thrombus, denoted by superscript s, is assumed to consist of a constrained mixture [27] of three constituents ξ: an amorphous ground substance matrix ($\xi = g$), a fibrin network ($\xi = f$), and fibrillar collagen ($\xi = c$). Their kinematics are constrained such that $\boldsymbol{v}^\xi = \boldsymbol{v}^s$, where $\boldsymbol{v}^\xi$ and $\boldsymbol{v}^s$ denote the velocity of each solid constituent ξ and the total solid s, respectively. We account for growth and remodeling of thrombus by modeling chemical reactions between the "solutes" plasmin(ogen) and (myo)fibroblasts and the solid constituents fibrin and collagen. The addition/subtraction of mass of an individual structural constituent may thus be expressed via a mass exchange term in the statement of mass balance, namely

$$\frac{\mathrm{D}\rho_r^\xi}{\mathrm{D}t} = \hat{\rho}_r^\xi, \quad \text{where } \xi = g, f, c, \tag{1}$$

where $\mathrm{D}\{\circ\}/\mathrm{D}t$ denotes the material time derivative, ρ_r^ξ is the current apparent mass density with respect to a reference volume, and $\hat{\rho}_r^\xi$ denotes the apparent mass density supply, also with respect to the reference volume. In our model, two mechanisms contribute to $\hat{\rho}_r^\xi$: first, we consider a decrease in mass density of fibrin due to degradation by plasmin(ogen) and, second, an increase in mass density of collagen by (myo)fibroblast deposition. These reactions will be discussed in more detail later.

2.2 Plasmin(ogen) and (Myo)fibroblasts

We assume that plasmin(ogen) ($\iota = pl$) is capable of transport via diffusion and advection; it can also react with fibrin. We further assume that (myo)fibroblasts ($\iota = fb$) are capable of migration and deposit collagen. For ease of computation, we treat both as "solutes" denoted by superscript ι. Mass balance for these constituents can be written

$$J^{-1}\frac{\mathrm{D}(J[1-\varphi^s]c^\iota)}{\mathrm{D}t} + \operatorname{div}\boldsymbol{j}^\iota = \left[1-\varphi^s\right]\hat{c}^\iota, \quad \text{with } \iota = pl, fb, \tag{2}$$

where $J = \det \boldsymbol{F}$ tracks changes in the volume of the mixture relative to its reference volume, φ^s is again the solid volume fraction, $\hat{c}^\iota$ is the mass exchange (i.e., molar supply or sink due to chemical reactions), and finally $\boldsymbol{j}^\iota$ is the molar flux relative to the solid.

2.3 Chemical Reactions

A key feature of our model is the ability of constituents to interact via chemical reactions, which contribute to lysis and maturation. In contrast to the common treatment of chemical kinetics, we introduce the deformation gradient $\boldsymbol{F}$ in addition to the standard state variables, which are concentrations c^ι of solutes and apparent referential densities ρ_r^ξ of solid constituents. It proves convenient to express apparent referential mass densities as concentrations through $c^\xi = \rho_r^\xi/[J-\varphi_r^s]M^\xi$, with φ_r^s the referential solid volume fraction and M^ξ the molar mass of constituents ξ. During lysis and maturation of thrombus, we consider all reactions to follow the law of forward mass action, viz. $\sum_\alpha \nu_R^\alpha \mathcal{E}^\alpha \rightarrow \sum_\alpha \nu_P^\alpha \mathcal{E}^\alpha$, where $\mathcal{E}^\alpha$ are the chemical species that correspond to constituents α ($= \xi$ or ι) and ν_R^α and ν_P^α are the

stoichiometric coefficients of reactant and product, respectively. Therefore, the molar supply $\hat{c}^\alpha$ of solid constituents and solutes may be expressed as $\hat{c}^\alpha = [\nu_P^\alpha - \nu_R^\alpha]\hat{\zeta}$, with

$$\hat{\zeta} = k\big(\boldsymbol{F}, c^\alpha\big) \prod_\alpha \big[c^\alpha\big]^{\nu_R^\alpha}, \quad \text{with } \alpha = \xi, \iota, \tag{3}$$

where $k(\boldsymbol{F}, c^\alpha)$ is the specific reaction rate. The balance of mass of the solid constituents, solutes, and the mixture may now be rewritten in terms of (3), see [7].

2.4 Interstitial Fluid

Interstitial fluid (mainly water, denoted by superscript w) is modeled as incompressible and inviscid, while frictional losses between the fluid and the solid matrix are included via a momentum exchange term within the statement of linear momentum balance [5]. By neglecting the volume fraction of the solutes, we may express the flux of interstitial fluid as $\boldsymbol{w} = [1 - \varphi^s][\boldsymbol{v}^w - \boldsymbol{v}^s]$, where φ^s is the solid volume fraction.

With the introduction of $\boldsymbol{w}$, the statement of mass balance for the entire mixture can be written

$$\operatorname{div}\big(\boldsymbol{v}^s + \boldsymbol{w}\big) = \sum_\alpha \frac{\hat{\rho}^\alpha}{\rho_T^\alpha}, \quad \text{with } \alpha = \xi, \iota, \tag{4}$$

where ρ_T^α is the true density of constituent α (current mass of constituent α divided by current volume of constituent α).

2.5 Balance of Linear Momentum

Given the expression for the total Cauchy stress, $\boldsymbol{\sigma} = -p\boldsymbol{I} + \boldsymbol{\sigma}^s$, where $\boldsymbol{\sigma}^s$ is the solid matrix stress, we can further write the spatial balance of linear momentum of the total mixture as

$$\operatorname{div}\boldsymbol{\sigma} = -\operatorname{grad} p + \operatorname{div}\boldsymbol{\sigma}^s = \boldsymbol{0}, \tag{5}$$

and where we assume quasi-static conditions.

2.6 Finite Element Implementation

The governing equations of the reactive mixture are solved using a nonlinear finite element method [35]. To this end, we express the initial-boundary value problem in weak form, which can be solved monolithically and fully implicitly using Newton's method. The first two equations that enter the statement of virtual work are the mass balance for each solute, (2), and mass balance of the mixture, (4). Adding the balance of linear momentum for the solid-fluid mixture, (5), complements the set of governing differential equations that lead to the solution of our variables of interest, the nodal displacement for the solids $\boldsymbol{u}$, the interstitial fluid pressure p, and the solute concentrations c^ι. Because the interstitial fluid pressure p is not guaranteed to be continuous across element boundaries, we instead solve for an effective fluid pressure $\tilde{p}$ that is continuous across element boundaries, where $\tilde{p} = p - R\theta\Phi\sum_\iota c^\iota$, R the universal gas constant, θ the absolute temperature, and Φ the osmotic coefficient. Importantly, c^ι is only continuous across element boundaries in the case of ideal solubility, which we assume here. Because the referential apparent mass densities of the solid constituents fibrin and collagen can be obtained by simple integration of (1) they

enter the statement of virtual work directly. With all this said, the total statement of virtual work

$$\begin{aligned}\delta W = &\sum_{\iota}\int_b \delta c^{\iota}\big[J^{-1}\mathrm{D}^s\big(J\big(1-\varphi^s\big)c^{\iota}\big)/\mathrm{D}t + \operatorname{div}\boldsymbol{j}^{\alpha}\big]\mathrm{d}v\\ &-\bar{\mathcal{V}}\int_b \delta\tilde{p}\big[1-\varphi^s\big]\hat{\zeta}\,\mathrm{d}v - \sum_{\iota} v^{\iota}\int_b \delta c\big[1-\varphi^s\big]\hat{\zeta}\,\mathrm{d}v\\ &+\int_b \delta\boldsymbol{v}\cdot\operatorname{div}\boldsymbol{\sigma}\,\mathrm{d}v + \int_b \delta\tilde{p}\operatorname{div}\big(\boldsymbol{v}^s+\boldsymbol{w}\big)\mathrm{d}v,\end{aligned} \tag{6}$$

where $\delta\boldsymbol{v}$ is a virtual velocity vector, $\delta\tilde{p}$ is a virtual effective interstitial pressure, δc^{ι} is a virtual molar energy, and $\bar{\mathcal{V}} = \sum_{\alpha} v^{\alpha}\mathcal{V}^{\alpha}$ with $\mathcal{V}^{\alpha} = M^{\alpha}/\rho_T^{\alpha}$ the molar volume. Integrations are over current mixture volume, v.

Expressions for the volumetric fluid flux $\boldsymbol{w}$ and solute molar fluxes $\boldsymbol{j}^{\iota}$ follow from inversion of the balances of linear momentum for the interstitial fluid and the "solutes" and result in a generalized Darcy's law and Fick's law, respectively. In addition, constitutive relations are required for the solid portion of the thrombus, mass forward reaction equations, and mechanically dependent permeability and diffusivity tensors, which we define in the following section.

3 Illustrative Constitutive Relations

3.1 Solid Matrix

We postulate the existence of a strain energy function $\mathcal{W}$ that determines the constitutive behavior of the solid constituents. Specifically, we describe the solid matrix as a constrained mixture of an isotropic ground substance $\mathcal{W}^g$ and an anisotropic fibrous matrix that may be populated with fibrin $\mathcal{W}^f$ or collagen $\mathcal{W}^c$, namely

$$\mathcal{W} = \mathcal{W}^g + \mathcal{W}^f + \mathcal{W}^c. \tag{7}$$

$\mathcal{W}^f$ and $\mathcal{W}^c$ are sensitive to decreases and increases in fiber density due to degradation and deposition, respectively. Fibers are deposited into extant matrix at a physiological prestretch. Hence, the total stretch of a fiber at the current time results multiplicatively from the stretch of the mixture in the direction of that fiber, the inverse of the mixture stretch at the time of deposition, and the deposition stretch value [8]. Thus, the total strain energy of the matrix follows from the integral over all active fibers based on their respective deposition times and individual reference configurations.

Specifically, we model the ground substance as neo-Hookean parameterized with Lamé parameters μ and λ, namely

$$\mathcal{W}^g = \frac{\mu}{2}[I-3] - \mu\ln J + \frac{\lambda}{2}[\ln J]^2, \tag{8}$$

where $I = \boldsymbol{C} : \boldsymbol{I}$ is the first invariant of the right Cauchy-Green tensor, with $\boldsymbol{I}$ the second order identity tensor, and $J = \det\boldsymbol{F}$ again. We consider the fibrous matrix using continuous distributions functions integrated over the unit sphere having surface S [22, 30],

$$\mathcal{W}^m = \frac{1}{4\pi}\int_S\int_0^s \frac{\hat{\rho}_r^m(\phi,\psi,\tau)}{\rho_0^m}\bar{\mathcal{W}}^m(\phi,\psi,\tau)\mathrm{d}\tau\mathrm{d}\theta\mathrm{d}\Phi, \quad \text{where } m = f, c, \tag{9}$$

with s being the current thrombus evolution time and $\tau \in [0, s]$ the collagen deposition time.

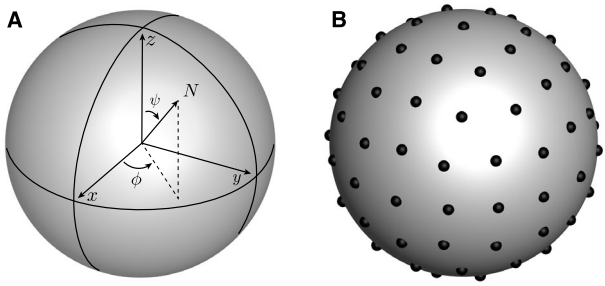

Fig. 1 (**A**) Parametrization of the fiber orientation vector $\boldsymbol{N}(\phi, \psi)$ within the unit sphere. (**B**) Discretization of the continuous spherical surface according to the fully symmetric cubature formula by Heo and Yuan [24] with 45 integration points over the half sphere. Adapted from [22]

Hence, each fiber contributes as a function of the mass densities of either fibrin or collagen, associated with the mass density production rate for that fiber, $\hat{\rho}_r{}^m(\phi, \psi)$, relative to a reference value ρ_0^m. In turn, the constitutive behavior of the unmodified fiber is described by a Fung-type strain energy function [25],

$$\bar{\mathcal{W}}^m(\phi, \psi, \tau) = \frac{k_1^m}{4k_2^m}\Big[\exp\Big(k_2^m\big[I\bar{V}^m(\phi, \psi, \tau) - 1\big]^2\Big) - 1\Big], \tag{10}$$

with the fiber direction-dependent invariant $I\bar{V}^m(\phi, \psi, \tau) = IV(\phi, \psi)IV(\phi, \psi, \tau)^{-1}IV_p^m$, where $IV(\phi, \psi) = \boldsymbol{C} : \boldsymbol{N}(\phi, \psi) \otimes \boldsymbol{N}(\phi, \psi)$ is the square of the current fiber stretch, $IV(\phi, \psi, \tau) = \boldsymbol{C}(\tau) : \boldsymbol{N}(\phi, \psi) \otimes \boldsymbol{N}(\phi, \psi)$ is the square of the fiber stretch at the time of deposition τ, and $IV_p^m = [\lambda_p^m]^2$ the deposition stretch squared. Note that $\boldsymbol{C} = \boldsymbol{F}^T\boldsymbol{F}$ and $\boldsymbol{C}(\boldsymbol{\tau}) = \boldsymbol{F}(\boldsymbol{\tau})^T\boldsymbol{F}(\boldsymbol{\tau})$ is the right Cauchy-Green tensor at time τ and $\boldsymbol{N}(\phi, \psi) = \{\cos\phi \sin\psi, \sin\phi \sin\psi, \cos\psi\}$ is the referential fiber direction vector.

Thus, as the referential apparent mass densities $\rho_r^m(\phi, \psi, s) = \int_0^s \hat{\rho}_r^m(\phi, \psi, \tau)\mathrm{d}\tau$, associated with individual fibrin or collagen fibers, evolve with time due to chemical reactions between fibrin and plasmin(ogen) or fibroblasts and collagen, the relative weights of the fiber contributions decrease for fibrin and increase for collagen. For practical purposes, the expression in (9) is integrated numerically and the time integral approximated, hence

$$\mathcal{W}^m = \sum_\beta \sum_t w^\beta \frac{\Delta\rho_r^{m,\beta,t}}{\rho_0^m}\bar{\mathcal{W}}^m\big(\boldsymbol{N}^\beta, t\big), \tag{11}$$

where $\Delta\rho_r^{m,\beta,t} = [\rho_r^{m,\beta,t} - \rho_r^{m,\beta,t-1}]$ and the directions $\boldsymbol{N}^\beta = \boldsymbol{N}(\phi^\beta, \psi^\beta)$ and weights w^β follow from a fully symmetric cubature formula by Heo and Yuan [24]. Specifically, we approximate the definite integral in (9) by 45 discrete directions and weights over the half sphere (Fig. 1), where the discrete times t coincide with converged time steps.

These constitutive relations were implemented in FEBio [35] via its plugin interface. To this end, our subroutine provides the Cauchy stress for the solid matrix $\boldsymbol{\sigma}^s = 2J^{-1}\boldsymbol{F}\partial\mathcal{W}/\partial\boldsymbol{C}\boldsymbol{F}^T$

$$\begin{aligned}\boldsymbol{\sigma}^s &= J^{-1}\mu[\boldsymbol{b} - \boldsymbol{I}] + J^{-1}\lambda \ln J\boldsymbol{I} \\ &\quad + 2J^{-1}\sum_m \sum_\beta \sum_t w^\beta \frac{\Delta\rho_r^{m,\beta,t}}{\rho_0^m} k_1^m\big[I\bar{V}^{m,\beta,t} - 1\big]\frac{IV_p^m}{IV^{\beta,t}}\exp\Big(k_2^m\big[I\bar{V}^{m,\beta,t} - 1\big]^2\Big)\boldsymbol{n}^\beta \otimes \boldsymbol{n}^\beta.\end{aligned} \tag{12}$$

Here, $\boldsymbol{b}$ is the left Cauchy-Green tensor and $\boldsymbol{n}^\beta$ are direction vectors in the spatial configuration, $\boldsymbol{n}^\beta = \boldsymbol{F}\boldsymbol{N}^\beta$. The spatial tangent $\mathfrak{c}^s = 4J^{-1}[\boldsymbol{F} \overline{\otimes} \boldsymbol{F}] : \partial^2\mathcal{W}/\partial\boldsymbol{C} \otimes \partial\boldsymbol{C} : [\boldsymbol{F}^T \overline{\otimes} \boldsymbol{F}^T]$, also implemented in the plugin, becomes

$$\mathbb{c}^s = J^{-1}\lambda \boldsymbol{I}\otimes\boldsymbol{I} + J^{-1}[\mu-\lambda\ln J]\mathbb{I} + 4J^{-1}\sum_m\sum_\beta\sum_t w^\beta \frac{\Delta\rho_r^{m,\beta,t}}{\rho_0^m} k_1^m\left[1+2k_2^m\left[\bar{IV}^{m,\beta,t}-1\right]^2\right]\left[\frac{IV_p^m}{IV^{\beta,t}}\right]^2 \times \exp\left(k_2^m\left[\bar{IV}^{m,\beta,t}-1\right]^2\right)\mathbb{N} \tag{13}$$

with the fourth order identity tensors $\mathbb{I} = [\boldsymbol{I}\,\overline{\otimes}\,\boldsymbol{I} + \boldsymbol{I}\underline{\otimes}\boldsymbol{I}]/2$ and the structural tensor $\mathbb{N} = \boldsymbol{n}^\beta\otimes\boldsymbol{n}^\beta\otimes\boldsymbol{n}^\beta\otimes\boldsymbol{n}^\beta$, where we used the short-hand $\{\circ\,\overline{\otimes}\,\bullet\}_{ijkl} = \{\circ\}_{ik}\{\bullet\}_{jl}$ as well as $\{\circ\underline{\otimes}\bullet\}_{ijkl} = \{\circ\}_{il}\{\bullet\}_{jk}$.

3.2 Reaction Rate Constitutive Behavior

Thrombus lysis and maturation are accounted for by considering chemical reactions involving the "solutes" plasmin(ogen) and (myo)fibroblasts and the solid constituents fibrin and collagen. Specifically, we consider two separate mass forward reactions. First, we model a reaction between fibrin and plasmin(ogen) to yield a reaction by-product. Because plasmin(ogen) is assumed to be constant (is not depleted), this is a pseudo first order reaction. Second, we consider a reaction between (myo)fibroblasts and nutrients to generate collagen. Here, nutrients and (myo)fibroblasts are also assumed to remain constant, making this equation a pseudo zeroth order reaction equation. For both types of reactions, we model the deformation-dependent specific reaction rate as

$$k^{m,\beta} = \epsilon k_0^m\left[IV^\beta\right]^\gamma, \quad \text{where } m = f, c, \tag{14}$$

where ϵ equals 1 in the case of fibrin and $[1-\rho_r^{c,\beta}/\rho_0^c]$ in the case of collagen, thus limiting the apparent referential mass density of the latter to a maximum allowable value ρ_0^c. Further, k_0^m is the specific reaction rate, IV^β the square of the fiber stretch ($IV^\beta = \boldsymbol{C}:\boldsymbol{N}^\beta\otimes\boldsymbol{N}^\beta$), and $\gamma\in\mathbb{W}$. Fibers under tension or compression may thus be degraded/deposited faster or slower depending on the value of γ [1, 11, 43].

This constitutive behavior was similarly implemented as a plugin in FEBio. To this end we provide $k^{m,\beta}$ and its derivative $\boldsymbol{k}^{m,\beta} = 2J^{-1}\boldsymbol{F}\partial k^{m,\beta}/\partial\boldsymbol{C}\,\boldsymbol{F}^T$, with

$$\boldsymbol{k}^{m,\beta} = 2J^{-1}\epsilon k_0^m\gamma\left[IV^\beta\right]^{\gamma-1}\boldsymbol{n}^\beta\otimes\boldsymbol{n}^\beta. \tag{15}$$

3.3 Mechanically Sensitive Permeability and Diffusivity

Transport of key biomolecules within the thrombus plays important roles in its lysis and maturation [17]. Such transport depends on the mechanical state of the thrombus, hence we model both plasmin(ogen) diffusivity and thrombus permeability as a function of deformation. Specifically, we assume an initially isotropic permeability tensor $\boldsymbol{p}$ and diffusivity tensor $\boldsymbol{d}^m$ as

$$\boldsymbol{p} = p_0\boldsymbol{I} + p_1 J^{-2}\boldsymbol{b} \tag{16}$$

and

$$\boldsymbol{d}^m = d_0^m\boldsymbol{I} + d_1^m J^{-2}\boldsymbol{b}, \quad \text{with } m = pl, fb, \tag{17}$$

respectively, where J is the Jacobian, $\boldsymbol{b}$ is the left Cauchy-Green tensor, and p_0, p_1, d_0^m, d_1^m are scalar material parameters. In addition, linearized permeability tensor, $\mathbb{p}$, and diffusivity

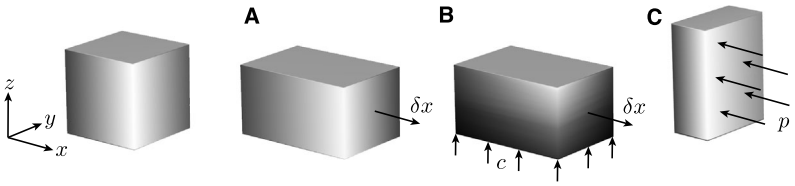

Fig. 2 Three different quarter symmetric loading scenarios for sensitivity study. (**A**) Strip biaxial extension (1.25:1 stretch ratio in x–y plane, traction free $z = 1$ surface) with homogeneous plasmin(ogen) and (myo)fibroblast distribution. (**B**) Same as (**A**) with diffusing plasmin(ogen) and migrating (myo)fibroblasts through the $z = 0$ surface. (**C**) Strip biaxial pressure (pressure applied to $x = 1$ surface, $y = 0$ surface is fixed in y-direction, traction free $z = 1$ surface) with homogeneous plasmin(ogen) and (myo)fibroblast distribution

tensor, $\mathbb{d}^m$, are

$$\mathbb{p} = p_0 \boldsymbol{I} \otimes \boldsymbol{I} - 2p_0 \mathbb{I} - p_1 J^{-2} \boldsymbol{b} \otimes \boldsymbol{I} \tag{18}$$

and

$$\mathbb{d}^m = d_0 \boldsymbol{I} \otimes \boldsymbol{I} - 2d_0^m \mathbb{I} - d_1^m J^{-2} \boldsymbol{b} \otimes \boldsymbol{I}, \quad \text{where } m = pl, fb. \tag{19}$$

Here, $\mathbb{I}$ is again the fourth order identity tensor, $\mathbb{I} = [\boldsymbol{I} \overline{\otimes} \boldsymbol{I} + \boldsymbol{I} \underline{\otimes} \boldsymbol{I}]/2$.

3.4 Sensitivity Study

Our model considers the mechanically mediated interplay among solid and fluid constituents as well as cellular and molecular "solutes". In a set of simple numerical experiments we demonstrate the sensitivity of our model to critical parameters and constitutive relations. Specifically, we consider three scenarios. First, we study separately fibrin-dominated and collagen-dominated unit cubes under displacement-driven strip biaxial extension (Fig. 2A). In this set of simulations, both cubes are instantaneously saturated with plasmin(ogen) or (myo)fibroblasts that homogeneously degrade fibrin and deposit collagen, respectively. During a second set of experiments, we apply the same mechanical boundary conditions, but study fibrin degradation and collagen deposition in response to plasmin(ogen) diffusion and (myo)fibroblast migration through the $z = 0$ surface of the cube (Fig. 2B). In the third set of experiments, we model the same unit cubes but apply biaxial stresses instead of displacement-driven biaxial extension (Fig. 2C). For all simulations, free fluid flow is allowed through the $z = 1$ surface of the material cube.

Because degradation follows a pseudo first-order reaction equation (i.e. plasmin(ogen) is not consumed during the reaction), we report the evolution of fibrin apparent referential density as a function of normalized time, using the time constant $\tau^f = [k_0^f \cdot c^{pl}]^{-1}$, where, k_0^f is the specific degradation reaction rate and c^{pl} is the concentration of plasmin(ogen). Similarly, we present the deposition of collagen referential apparent density as a function of normalized time, with time constant $\tau^c = [k_0^c \cdot c^{fb}/c^c]^{-1}$, where k_0^c is the specific deposition reaction rate, c^{fb} is the (myo)fibroblast "concentration", and c_0^c is the maximum allowable collagen concentration. All remaining parameter values are listed in Table 1.

Using our first model problem, Figs. 3A, B illustrate the sensitivity of the apparent referential fibrin and collagen density to parameter γ (recall equation (14)). Increasing γ increases the degradation rate since the reaction rate parameter k^f is amplified through its

Table 1 Parameters in sensitivity study and simulation of occlusive venous thrombus. Values were estimated from references or chosen when no data was available

Symbol	Description	Value	Unit	Reference
Thrombus/Wall geometry				
	Thrombus length	4.0	mm	[32]
	Thrombus diameter	1.2	mm	[32]
	Venous wall length	8.0	mm	[–]
	Venous wall thickness	0.1	mm	[–]
Thrombus material				
φ_0	Initial solid volume fraction	0.2	–	[17]
μ	Ground substance shear modulus	0.0038	MPa	[–]
λ	Ground substance Lamé parameter	0.058	MPa	[–]
k_1^f	Fibrin material parameter	0.01	MPa	[–]
k_2^f	Fibrin material parameter	0.0	–	[–]
k_1^c	Collagen parameter	1.031	MPa	[–]
k_2^f	Collagen parameter	6.559	–	[–]
T^a	Platelet tension parameter	$1.6e^{-4}$	MPa	[14]
λ_p^f	Fibrin deposition stretch	1.00	–	[–]
λ_p^c	Collagen deposition stretch	1.04	–	[10]
Venous wall material				
	Wall shear modulus	0.1	MPa	[31]
	Wall bulk modulus	1000	MPa	[–]
λ^z	Axial prestretch	1.7	–	[31]
Solid and solute constituents				
M^f	Fibrin molecular mass	340	kDa	[19]
M^c	Collagen molecular mass	285	kDa	[26]
M^{pl}	Plasminogen molecular mass	80	kDa	[9]
M^{fb}	(Myo)fibroblast molecular mass	80	kDa	[–]
c_0^{pl}	Initial plasmin(ogen) concentration	$1.875e^{-4}$	nmol/mm^3	[42]
c^{pl}	Blood plasmin(ogen) concentration	$2.5e^{-3}$	nmol/mm^3	[42]
c^{fb}	Wall (myo)fibroblast concentration	$1.0e^{-8}$	nmol/mm^3	[–]
Transport				
p_0	Permeability parameter	0.0	mm^4/N/s	[–]
p_1	Permeability parameter	0.91	mm^4/N/s	[3]
d_0^{pl}	Plasminogen diffusivity parameter	$2.5e^{-3}$	mm^2/s	[37]
d_1^{pl}	Plasminogen diffusivity parameter	$0.5e^{-4}$	mm^2/s	[37]
d_0^{fb}	(Myo)fibroblast diffusivity parameter	$5.0e^{-8}$	mm^2/s	[–]
d_1^{fb}	(Myo)fibroblast diffusivity parameter	0.0	mm^2/s	[–]
Reactions				
k_0^f	Specific fibrin degradation rate	$2.0e^{-4}$	1/s	[–]
k_0^c	Specific collagen deposition rate	5.0	1/s	[–]
γ^f	Fibrin degradation rate exponent	1.0	–	[–]
γ^c	Collagen deposition rate exponent	1.0	–	[–]

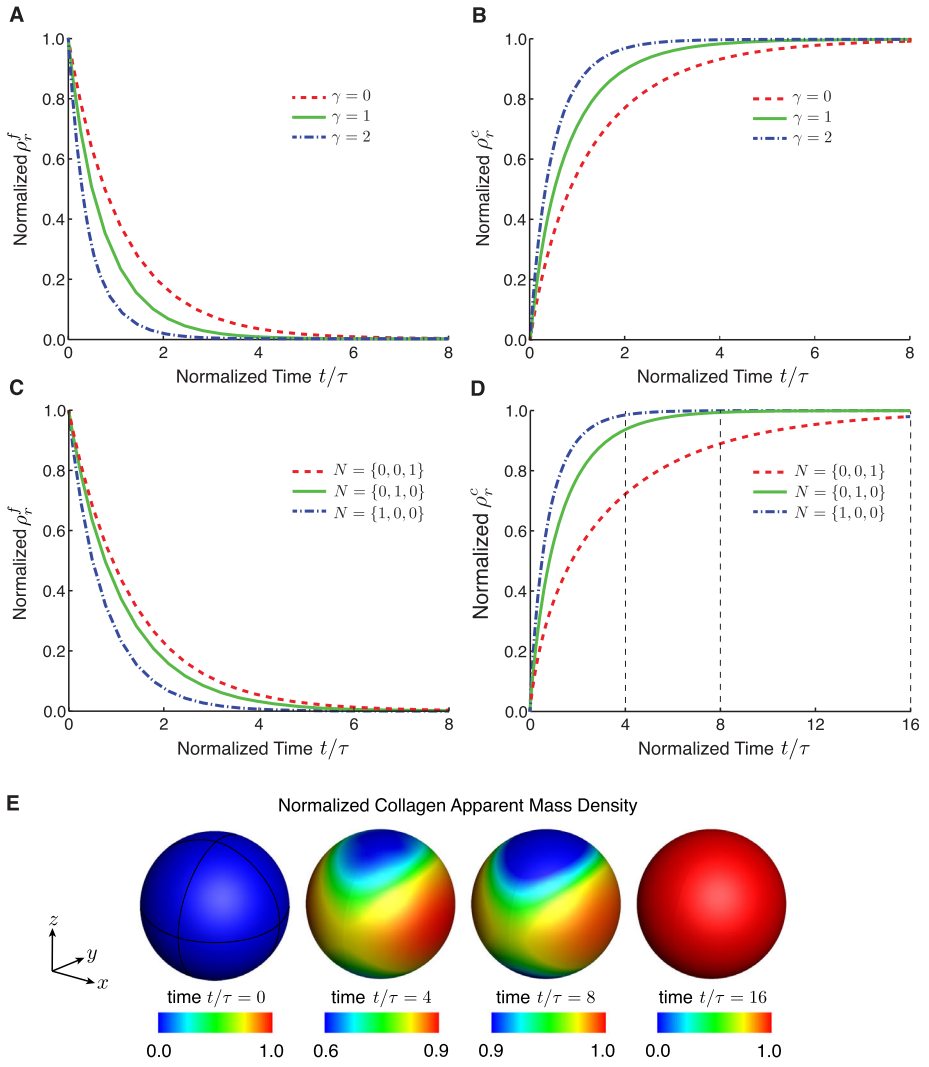

Fig. 3 Fibrin degradation rate and collagen deposition rate depend on the solid deformation in a direction dependent manner. (**A**) Fibrin degradation rate is accelerated by increasing γ through dependence on the pseudo invariant IV^{γ}. (**B**) Collagen deposition rate is accelerated by increasing γ through dependence on the pseudo invariant IV^{γ}. (**C**) Fibrin degradation rate varies with direction $\boldsymbol{N}$ and is the highest in first principal loading direction and the lowest in third principal loading direction. (**D**) Collagen deposition rate varies with direction $\boldsymbol{N}$ and is the highest in first principal loading direction and the lowest in third principal loading direction. (**E**) Anisotropic collagen deposition as a function of deformation at four times (see **D** for comparison), where density distributions reflect the principal load directions. Note, continuous distributions are obtained through cubic interpolation of 45 integration points over the half sphere using symmetry conditions. Further note, in (**E**), we chose different color scales to highlight remodeling induced material anisotropy

dependence on the pseudo invariant IV to the power of γ (Fig. 3A). Similarly, collagen deposition accelerates with increasing γ, as shown in Fig. 3B. We further observe that for $\gamma = 1$ the non-equibiaxial loading causes spatial variations in fibrin degradation as well as collagen deposition rates that result in load-induced material anisotropy (Fig. 3C, D). In

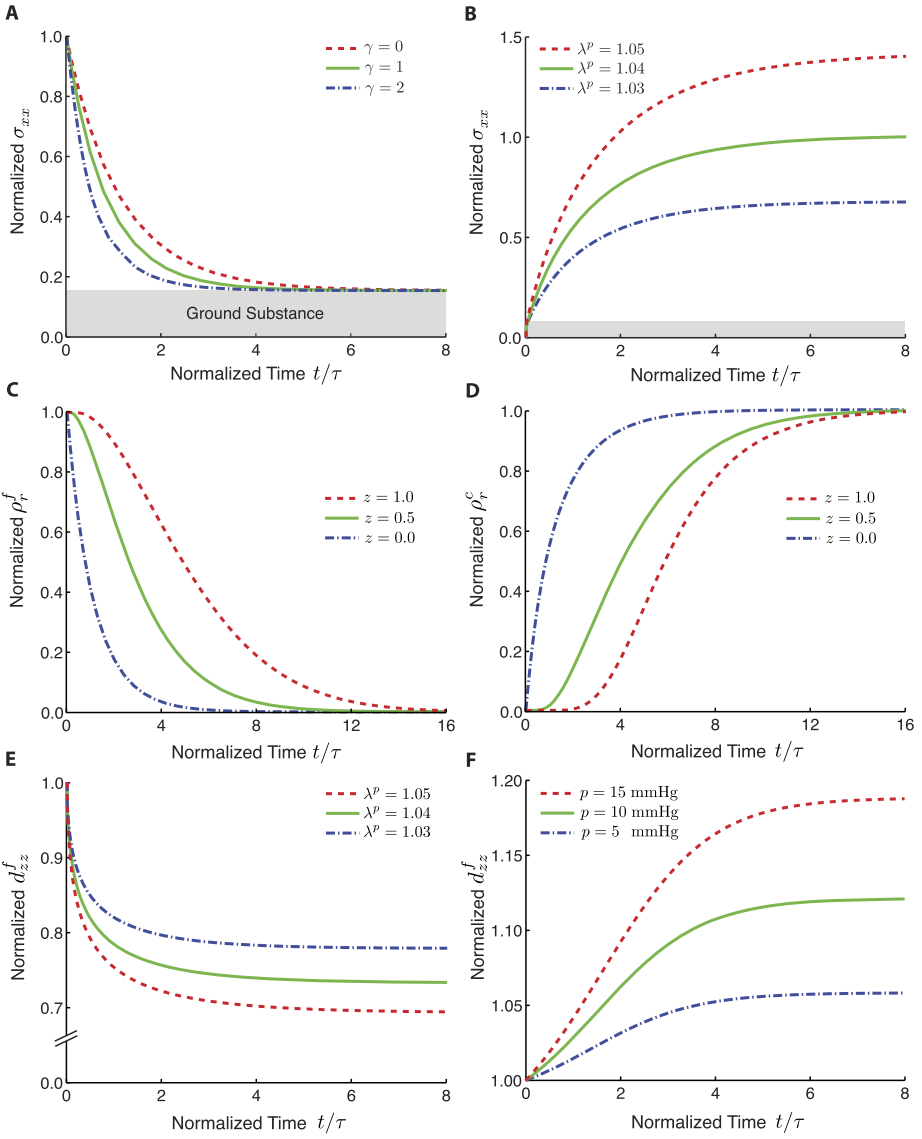

Fig. 4 Fibrin degradation and collagen deposition affect material stiffness: (**A**) Degradation reduces the material stiffness and thus the state of stress via removal of fibrin as a function of γ. (**B**) Collagen deposition increases material stiffness, wherein a larger collagen prestretch increases the equilibrium value. Transport induced material heterogeneity: (**C**) Intra-thrombus transport of plasmin(ogen) delays fibrin degradation and thus results in spatially varying fibrin densities. (**D**) (Myo)fibroblast migration delays collagen deposition and thus results in spatially varying collagen densities. Mechanical sensitivity of plasmin(ogen) diffusivity: (**E**) Plasmin(ogen) diffusivity decreases with thrombus contraction as a function of collagen prestretch. (**F**) Plasmin(ogen) diffusivity increases under pressure and is sensitive to pressure magnitude

Fig. 3E this anisotropy is further illustrated at one representative material point (of the homogenous unit cube). Here, evolving collagen density is interpolated over the unit sphere, based on the 45 discrete fiber directions (Fig. 1B).

As the microstructure of the thrombus evolves during fibrin degradation and collagen deposition, its state of stress also changes. Where fibrin is initially the primary load carrying component, its degradation results in reduced stiffness (Fig. 4A). Once all fibrin is degraded (and in the case of no collagen deposition), the ground substance provides the only remaining resistance to stretch. On the other hand, Fig. 4B illustrates that the state of stress of collagen dominated sample strongly depends on the deposition stretch of the collagen fibers. Specifically, collagen deposited at a higher stretch results in increased equilibrium stress.

In Fig. 4C, D we illustrate our second scenario (Fig. 2B) in which plasmin(ogen) enters and (myo)fibroblasts invade the biaxially stretched sample through the $z = 0$ surface. A diffusivity and migration mediated delay of plasmin(ogen) and (myo)fibroblasts, respectively, results in early fibrin degradation and early collagen deposition at $z = 0$ and late degradation and deposition at $z = 1$. Thus, material inhomogeneities naturally emerge from inclusion of thrombus transport phenomena such as diffusion and migration.

Mechanically altered intra-thrombus transport through diffusion and advection is critical to both thrombus lysis and maturation. We implement these effects via stretch dependence of the diffusivity and permeability tensors, see equations ((16)–(17)). Figure 4E, F demonstrate the model's sensitivity to degradation and deposition by means of the z-component of the plasmin(ogen) diffusivity tensor. Using the first loading scenario (Fig. 2A), we see that diffusivity may vary with collagen deposition stretch (Fig. 4E). As collagen deposition stretch is increased, thrombus compaction in the z-direction results in decreasing diffusivity, thus coupling progressive collagen deposition to reduced plasmin(ogen) transport and thus decreasing fibrin degradation. Similarly, using our third loading scenario (Fig. 2C) we see that decreasing fibrin density results in increased compression under stress in the planar directions and thus increased out-of-plane sample extension. Positive stretch in the z-direction subsequently increases diffusivity and provides a positive feedback for fibrin degradation via an increased plasmin(ogen) supply (Fig. 4F). These examples show that intra-thrombus transport may be increased or decreased by fibrin degradation and collagen deposition, respectively, and thus may be accelerated or decelerated through mechanically mediated feedback mechanisms.

4 Remodeling Venous Thrombus

We now combine all aspects of our proposed model in a three dimensional simulation of an occlusive venous thrombus. Specifically, we begin our simulation once the fibrin network has mostly developed (minutes to hours after initiation). Consequently, we assume that no additional fibrin deposition occurs. Starting from this point, we consider the transport of plasmin(ogen) from the thrombus/blood interface and associated degradation of the existing fibrin network by plasmin(ogen) as well as the migration of (myo)fibroblasts from the thrombus/wall interface and associated deposition of collagen during maturation. We also include the venous wall in our simulations. Specifically, we model the wall as neo-Hookean and use a three-field finite element interpolation scheme to approximate its nearly incompressible material behavior. We also include axial prestretch in our venous wall model. To this end, we assume that our reference configuration is not stress-free, but is rather the result of an isochoric deformation from a fictitious unloaded configuration according to a prestretch tensor $\boldsymbol{F}^z = \lambda^z \boldsymbol{N}^z \otimes \boldsymbol{N}^z + 1/\sqrt{\lambda^z}[\boldsymbol{I} - \boldsymbol{N}^z \otimes \boldsymbol{N}^z]$, where λ^z is the axial prestretch and $\boldsymbol{N}^z$ is the axial direction vector [39]. Lastly, we implement an additive active stress model to include thrombus compaction resulting from platelet activation and contraction. Thus,

we add the active stress tensor $\boldsymbol{\sigma}^a$ to the solid stress tensor, where $\boldsymbol{\sigma}^a = T^a \boldsymbol{b}$, with T^a the tension parameter and $\boldsymbol{b}$ is the left Cauchy-Green deformation tensor.

Because there are few specific data on the evolution of human venous thrombus, we base our computational model largely on observations and measurements from a well-accepted stasis deep vein thrombosis mouse model [18]. Toward this end, we surgically ligated the inferior vena cava just below the renal veins to initiate the formation of (relatively) large, cylindrical thrombus samples. At 2 and 4 weeks, we explanted the venous thrombus and used combined histology/immunohistochemistry and micro-uniaxial tensile testing to characterize the specimens [32]. We measured thrombus length and diameter, spatial fibrin and collagen distributions, (myo)fibroblast distribution and count, neutrophil and macrophage distribution and count, and quantified the uniaxial tensile stress-stretch behavior.

Based on these data, we first estimate the material parameters for our ground substance matrix (μ, λ) as well as those for the fibrin and collagen (k_1^f, k_2^f and k_1^c, k_2^c). To this end, we built virtual cylindrical thrombus samples at 2 weeks and 4 weeks based on geometric experimental data as well as relative distributions of fibrin and collagen: 4 mm length and 1.2 mm diameter at 2 weeks and 3 mm length and 0.7 mm diameter at 4 weeks, with relative ground substance:fibrin:collagen distributions of 1:7:2 and 1:0:9, respectively. Thus, at 2 weeks our thrombus material is dominated by fibrin with some early collagen deposition, while at 4 weeks our sample is dominated by collagen. Subsequently, we apply a trust-region algorithm to minimize an objective function that penalizes the sum of the squared differences between experimentally determined load-stretch curves and finite element simulations, simultaneously for the samples at 2 and 4 weeks. Furthermore, during initial simulations we iteratively adjusted the fibrin degradation rate, the collagen deposition rate, and the (myo)fibroblast migration rate to match our histological observations qualitatively. All other parameters are either literature values or were chosen for lack of available data, see Table 1.

Notwithstanding the single ligature, for computational ease, we apply venous blood pressure to the distal and proximal thrombus surfaces. In contrast, we model the distal and proximal surfaces of the venous segment as fixed in space. Without data to the contrary, we also model the thrombus and wall as perfectly adherent. Finally, while this model is fully three dimensional, in the interest of computational time, all simulations are carried out employing axisymmetric boundary conditions. The final geometry and mesh are shown in Fig. 6A.

Before simulating thrombus lysis and maturation, we apply mechanical as well as chemical initial conditions step-wise. In the first load step we apply venous blood pressure and wait for intra-thrombus fluid pressure to equilibriate. Secondly, we activate platelet contraction, and, again, let the thrombus pressure equilibrate. In the last initiating load step, we perfuse the thrombus homogeneously with an initial plasmin(ogen) concentration.

The actual simulation of thrombus evolution begins with the application of a blood-equivalent plasmin(ogen) concentration at the thrombus/blood interface and a count-down for (myo)fibroblast migration from the thrombus/wall interface, which begins at 7 days into the simulation. We end the simulation after 8 weeks of thrombus evolution. In Fig. 5 we show the resulting transport of plasmin(ogen) and the migration of (myo)fibroblasts as well as the evolution of fibrin referential apparent density and collagen referential apparent density at times 0 days, 1/8 days, 7 days, 14 days, 28 days, and 56 days.

The first row in Fig. 5 depicts the transport of plasmin(ogen) from the thrombus/blood interface. Recalling the initial uniform plasmin(ogen) concentration, subsequent transport of plasmin(ogen) from the thrombus/blood interface inward results in a concentration gradient, which we can still observe at 3 hours. After 7 days, this gradient vanishes as the entire thrombus is saturated with plasmin(ogen).

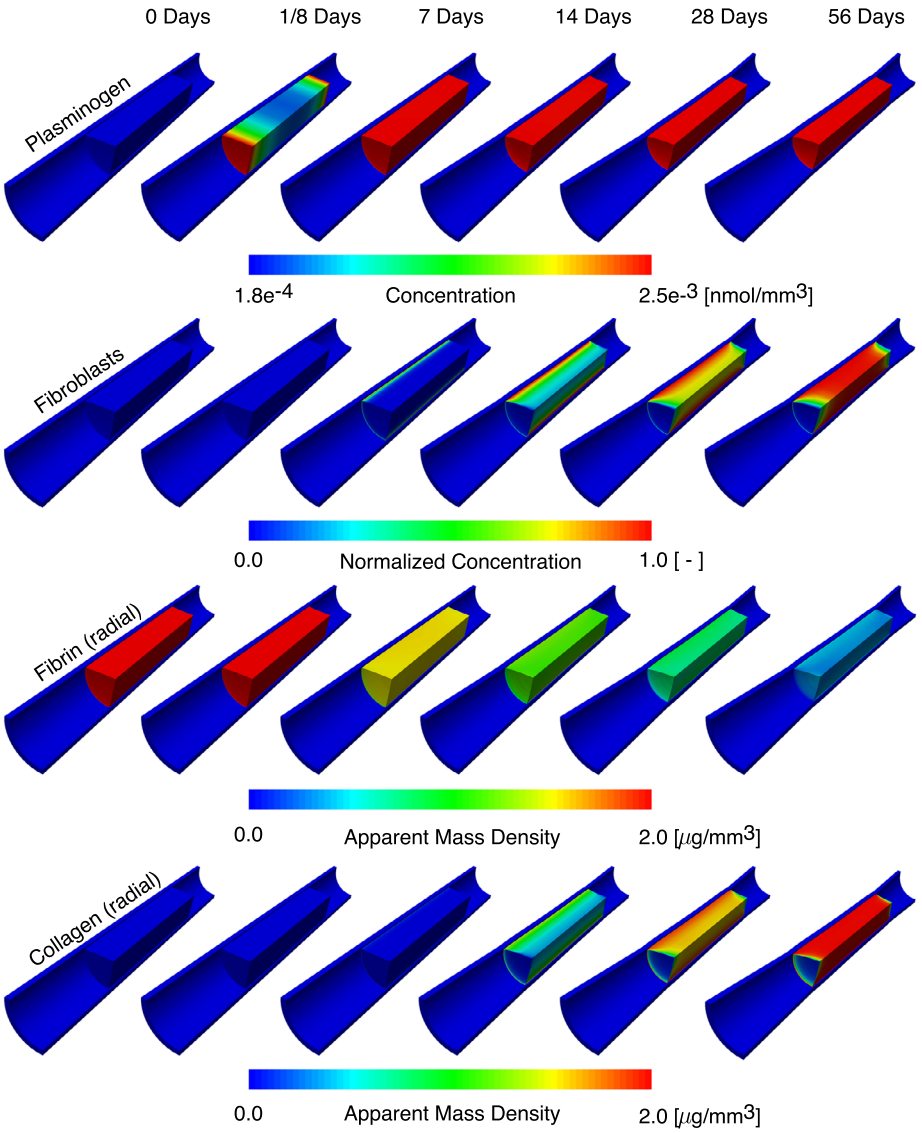

Fig. 5 Simulated occlusive venous thrombus remodeling. Between 0 days and 56 days differing time scales of plasmin(ogen) transport and (myo)fibroblast migration result in nearly homogeneous degradation of fibrin and heterogeneous deposition of collagen (shown are the results in radial direction). The simulated results match qualitatively our prior experimental observations [32]

In contrast, (myo)fibroblasts do not begin to invade the thrombus until day 7. As observed in our experimental data, these cells have made their way into the thrombus volume by day 14, with the highest "concentration" at the thrombus/wall interface and only few (myo)fibroblasts in the thrombus center. This picture changes by day 28 when the cells have substantially invaded the thrombus. By day 56 the entire thrombus is populated with (myo)fibroblasts with the exception of the distal and proximal thrombus surfaces which we exclude from (myo)fibroblast invasion due to its direct contact with blood.

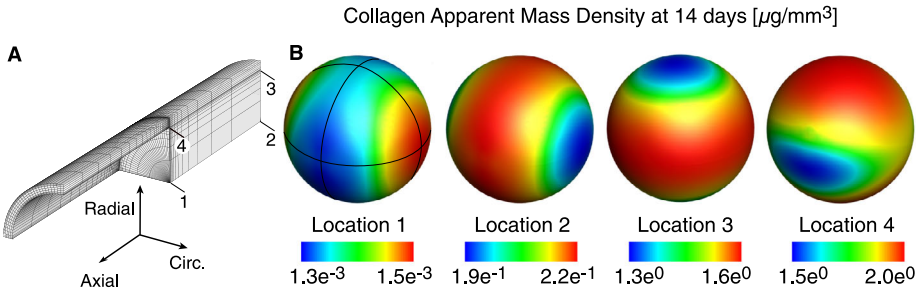

Fig. 6 (**A**) Quarter symmetric segment of thrombus/wall complex and finite element discretization. (**B**) Collagen distribution on microspheres at four different locations after 14 days reflects heterogeneous and anisotropic evolution of thrombus microstructure. Note, continuous distributions are obtained through cubic interpolation of 45 integration points over the half sphere using symmetry conditions. Further note, in (**B**) we chose different color scales to highlight remodeling induced material anisotropy

The different times scales of plasmin(ogen) diffusion and (myo)fibroblast migration are reflected in characteristically different evolution patterns between fibrin and collagen. Because plasmin(ogen) is transported at a high rate into the thrombus center, while the degradation rate of fibrin is relatively low, fibrin changes almost homogeneously throughout the thrombus volume. Fibrin density decreases asymptotically from 2 μg/mm^3 at 0–7 days to close to 0 μg/mm^3 at 56 days, see Fig. 5 for fibrin density in the radial direction. On the other hand, because the collagen deposition rate is relatively high in comparison to the (myo)fibroblast migration rate, collagen density mimics (myo)fibroblast density qualitatively. Collagen density further shows a clear gradient from the periphery toward the thrombus center line at 14 days, which vanishes at 28 days and 56 days when collagen has mostly replaced fibrin as the predominant structural constituent of thrombus.

Figure 6B depicts both the heterogeneity as well as the anisotropy of collagen evolution after 2 weeks of maturation. Collagen density varies considerably, as indicated by the different scales at four representative locations. In addition, variations over the unit sphere represent load-induced material anisotropy. At location 3, for example, we find that collagen is deposited predominantly in axial and circumferential directions and not in the radial direction, which reflects the time average of the principal load directions. This locally reduced deposition of collagen in the radial direction may further present a focal material weakness, potentially indicative of a subsequent failure point.

Changes in fibrin and collagen density are also reflected in changes in thrombus geometry. In the current problem, we apply traction boundary conditions to the distal and proximal thrombus surfaces (blood pressure), as well as to the thrombus peripheral boundary (venous wall). Thus, collagen deposition results in thrombus contraction rather than the increased equilibrium stresses that we saw in Fig. 4B. This contraction, consistent with the phenomenon of wound contraction, is depicted in contour plots of total displacement over time in Fig. 7. In this time sequence, we find at 0 days that venous blood pressure applied to the distal and proximal surface of the thrombus and platelet contraction results in compaction at the distal and proximal boundaries but negligible compaction at the radial boundary. Yet, because the thrombus is constrained to move with the venous wall, this displacement does not translate to the thrombus center. We see also slight increases in displacement at day 7 as fibrin degradation reduces thrombus' stiffness. Beginning at day 14 and continuing through day 56, we notice a clear compaction throughout the thrombus as a result of increased collagen deposition.

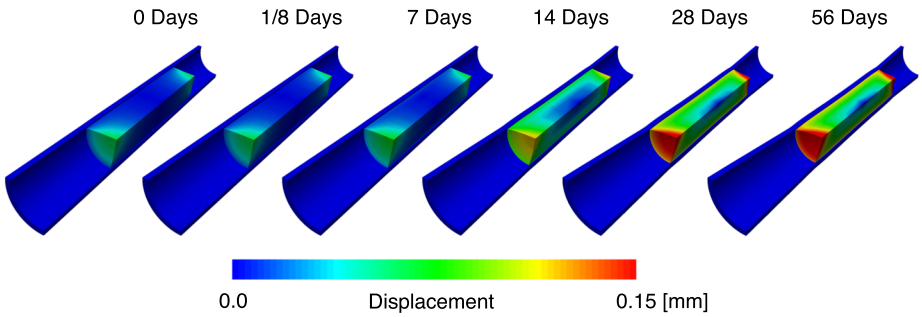

Fig. 7 Occlusive venous thrombus compaction. Between 0 days and 56 days venous blood pressure, platelet contraction, fibrin degradation and collagen deposition result in increased thrombus compaction over time. While blood pressure and platelet contraction dominate early compaction up to 7 days, late compaction is dominated by collagen deposition

5 Discussion

Thrombus plays a critical role in many diseases as well as clinical complications, including deep vein thrombosis [23], stroke [36], aortic dissections [48], abdominal aortic aneurysms [44], coronary disease [33], and medical device failure [45]. The complex multiscale/multiphysical phenomena defining thrombus lysis and maturation largely determine the progression of these diseases as well as their outcomes. Furthermore, thrombus lysis and maturation are targets of current treatments and therapeutic technologies [4]. Computational models may hold the potential to better understand thrombus evolution and thus many of the above diseases. Furthermore, computational models may serve as platforms for personalized treatment planning and therapeutic optimization.

Historically, the study of thrombus has largely focused on the biochemistry of thrombus initiation and formation [17, 51, 52]. The biochemomechanics of thrombus during long-term evolution has received less attention, with few exceptions [29]. Recently, however, it has become clear that biochemomechanics play an important role, not only in thrombus formation [16], but also during thrombus lysis or maturation [12, 13, 38, 50]. We introduced the first finite element framework to combine the nonlinear continuum mechanics of thrombus, intra-thrombus transport, and reactions among solids, interstitial fluid, and diffusing and migrating "solutes". By doing so, we unite biology and chemistry with mechanics on multiple scales. Specifically, we consider spatio-temporal changes in and interactions among biomolecular and cellular species and structural constituents and their consequences on the macroscopic mechanical behavior of thrombus. To the best of our knowledge, this is also the first use of the microsphere approach to model the anisotropically and heterogeneously remodeling microstructure of thrombus. We interpret the discrete quadrature derived directions representing the microspherical surface as fibrin and collagen bundles and allow each to remodel individually. Consequently, the anisotropic degradation of fibrin and deposition of collagen can be resolved, in our case, in 45 discrete directions. Thus, evolving material anisotropy and heterogeneities emerge naturally from our model rather than requiring a priori definition of growth tensors, as, for example, in finite growth theory [21, 40, 41].

The current framework was inspired by our recent report on the evolving histomechanics of venous thrombus in a deep vein thrombosis mouse model [32]. Combined histology/immunohistochemistry and uniaxial tensile test data revealed dramatic changes from 2 weeks to 4 weeks. In short, venous thrombus at 2 weeks is primarily a fibrin-based mesh

with relatively low stiffness, with abundant inflammatory cells throughout the thrombus but (myo)fibroblasts near the periphery of thrombus. By 4 weeks, however, (myo)fibroblasts were seen throughout the thrombus, co-localized with fibrillar collagen that likely was responsible for the significantly higher material stiffness at that time. That is, thrombus evolved significantly within a few weeks from a relatively compliant fibrin mesh to a stiff, collagenous pseudo-tissue, largely driven by the degradation of fibrin by plasmin and the invasion of (myo)fibroblasts that deposited collagen. Our numerical example of an occlusive venous thrombus (cf. Sect. 4) was informed by these observations on cell distributions, cell counts, and mechanical properties as a function of relative amounts of the structural constituents fibrin and collagen.

One of the challenges in the study of venous thrombus lysis or maturation lies in delineating the origin of diverging fates; thrombus in vivo may either lyse spontaneously or may mature into a chronic lesion. This outcome is critical from a clinical perspective because a lysing thrombus is more likely to embolize than a chronic thrombus. We hypothesize that thrombus fate may be determined by the competition between fibrin degradation and collagen deposition, with local differences likely critical. In this work we show that this competition may be partially determined through mechanically-mediated feedback mechanisms. For example, collagen deposition and subsequent thrombus contraction may reduce diffusion and advection of important thrombolytic biomolecules such as plasmin(ogen), thus slowing lysis and further promoting maturation.

Thrombus microstructure appears heterogeneous and anisotropic [32, 47]. To date, no model of thrombus remodeling has accounted for local differences in constituent density or spatially varying material properties. We employed the microsphere concept to allow thrombus to remodel freely in response to reactive interactions among solid, fluid, and "solute" constituents as a function of their locally and directionally varying mechanical environment. We believe that material heterogeneity and anisotropy may be critical to the fate of venous thrombus; local differences in collagen and fibrin density, for example, could account for different failure modes such that advanced lysis or reduced maturation at the thrombus wall interface may result in whole thrombus dislodgement, while homogeneous degradation may result in thrombus fragmentation and smaller emboli. In our simulation, an occlusive venous thrombus remodeled in a heterogeneous, anisotropic fashion. For example, collagen deposition at the thrombus wall interface is minimal in the radial direction, which, under the radial forces of thrombus contraction, could increase the risk for thrombus detachment and subsequent embolization. Microstructural studies of occlusive venous thrombus at varying stages of remodeling will be needed to confirm this hypothesis, which likely would need refinement if one accounts for remodeling of the underlying vascular wall as well.

While venous thrombus and arterial thrombus are often treated separately (e.g., white thrombus (arterial) and red thrombus (venous)), it is becoming increasingly clear that they represent two observations from a continuous disease spectrum [28]. Therefore, our model, with appropriate extensions, may also be applicable to arterial thrombus. Our particular interest on the arterial side lies in the study of thrombus in aortic aneurysms and dissections. Here we suspect thrombus may play a dual role. On one hand, thrombus may be protective, shielding the adjacent aortic wall. On the other hand, it may serve as source of biological (proteolytic) activity that could promote the progressive break-down of aortic wall constituents and ultimately contribute to wall rupture. Our computational model of the biochemomechanics of occlusive thrombus (with appropriate extensions) may similarly aid in testing these hypotheses. Lastly, considering the important physiological role of thrombus in hemostasis following vascular injury, it is not surprising that thrombus evolution closely resembles the wound healing response. Our work may, thus, also be relevant to the study of wound healing [46].

Of course our model depends on a number of assumptions, parameters, and constitutive relations that are currently either only partially known or unknown. For example, no data are available on the evolving porosity of venous thrombus, the mechanical dependence of thrombus permeability, or the mechanical dependence of plasmin(ogen) diffusivity. Similarly, we currently do not have a three dimensional model of platelet contraction and do not know the mathematical form of mechanically dependent reaction equations, or the mechanical properties of venous thrombus under compression at various stages of evolution. Other limitations include our choice to neglect interactions among multiple migrating cell species, focus on plasmin(ogen) but not fibrin(ogen), and the potential evolution of the venous wall, all of which may affect thrombus properties. Further, we currently assume perfect adherence between thrombus and venous wall, which is an approximation of the actual interfacial properties at best. Based on the data we have available, however, we consider the present work another step toward a general framework that includes important biological, chemical, and mechanical contributors to thrombus lysis or maturation.

Acknowledgements This work was funded, in part, by NIH grants R01 HL086418, U01 HL116323, and T32 HL007974. We also thank Steve Maas and David Rawlins for their invaluable help with the implementation of our constitutive laws in FEBio and Professor Gerard Ateshian for his input and support.

References

1. Adhikari, A.S., Chai, J., Dunn, A.R.: Mechanical load induces a 100-fold increase in the rate of collagen proteolysis by MMP-1. J. Am. Chem. Soc. **133**(6), 1686–1689 (2011)
2. Adhikari, A.S., Mekhdjian, A.H., Dunn, A.R.: Strain tunes proteolytic degradation and diffusive transport in fibrin networks. Biomacromolecules **13**(2), 499–506 (2012)
3. Adolph, R., Vorp, D.A., Steed, D.L., Webster, M.W., Kameneva, M.V., Watkins, S.C.: Cellular content and permeability of intraluminal thrombus in abdominal aortic aneurysm. J. Vasc. Surg. **25**(5), 916–926 (1997)
4. Alexandrov, A.V., Molina, C.A., Grotta, J.C., Garami, Z., Ford, S.R., Alvarez-Sabin, J., Montaner, J., Saqqur, M., Demchuk, A.M., Moyé, L.A., et al.: Ultrasound-enhanced systemic thrombolysis for acute ischemic stroke. N. Engl. J. Med. **351**(21), 2170–2178 (2004)
5. Ateshian, G.A., Albro, M.B., Maas, S., Weiss, J.A.: Finite element implementation of mechanochemical phenomena in neutral deformable porous media under finite deformation. J. Biomech. Eng. **133**(8), 081005 (2011)
6. Ateshian, G.A., Maas, S., Weiss, J.A.: Multiphasic finite element framework for modeling hydrated mixtures with multiple neutral and charged solutes. J. Biomech. Eng. **135**(11), 111001 (2013)
7. Ateshian, G.A., Nims, R.J., Maas, S., Weiss, J.A.: Computational modeling of chemical reactions and interstitial growth and remodeling involving charged solutes and solid-bound molecules. Biomech. Model. Mechanobiol. **13**(5), 1105–1120 (2014)
8. Baek, S., Rajagopal, K., Humphrey, J.: A theoretical model of enlarging intracranial fusiform aneurysms. J. Biomech. Eng. **128**(1), 142–149 (2006)
9. Barlow, G.H., Summaria, L., Robbins, K.C.: Molecular weight studies on human plasminogen and plasmin at the microgram level. Int. J. Biol. Chem. **244**(5), 1138–1141 (1969)
10. Bersi, M.R., Bellini, C., Wu, J., Montaniel, K.R., Harrison, D.G., Humphrey, J.D.: Excessive adventitial remodeling leads to early aortic maladaptation in angiotensin-induced hypertension. Hypertension **67**(5), 890–896 (2016)
11. Breen, E.C.: Mechanical strain increases type I collagen expression in pulmonary fibroblasts in vitro. J. Appl. Physiol. **88**(1), 203–209 (2000)
12. Brown, A.E., Litvinov, R.I., Discher, D.E., Purohit, P.K., Weisel, J.W.: Multiscale mechanics of fibrin polymer: gel stretching with protein unfolding and loss of water. Science **325**(5941), 741–744 (2009)
13. Bucay, I., O'Brien, E.T. III, Wulfe, S.D., Superfine, R., Wolberg, A.S., Falvo, M.R., Hudson, N.E.: Physical determinants of fibrinolysis in single fibrin fibers. PLoS ONE **10**(2), e0116 (2015)
14. Cohen, I., Gerrard, J.M., White, J.G.: Ultrastructure of clots during isometric contraction. J. Cell Biol. **93**(3), 775–787 (1982)
15. Davie, E.W., Fujikawa, K., Kisiel, W.: The coagulation cascade: initiation, maintenance, and regulation. Biochemistry **30**(43), 10363 (1991)

16. Di Achille, P., Tellides, G., Figueroa, C., Humphrey, J.: A haemodynamic predictor of intraluminal thrombus formation in abdominal aortic aneurysms. Proc. R. Soc. A **470**(2172), 20140 (2014). 163
17. Diamond, S.L., Anand, S.: Inner clot diffusion and permeation during fibrinolysis. Biophys. J. **65**(6), 2622 (1993)
18. Diaz, J.A., Obi, A.T., Myers, D.D., Wrobleski, S.K., Henke, P.K., Mackman, N., Wakefield, T.W.: Critical review of mouse models of venous thrombosis. Arterioscler. Thromb. Vasc. Biol. **32**(3), 556–562 (2012)
19. Doolittle, R.F.: Fibrinogen and fibrin. Encyclopedia of Life Sciences (2001)
20. Emelianov, S., Chen, X., O'Donnell, M., Knipp, B., Myers, D., Wakefield, T., Rubin, J.: Triplex ultrasound: elasticity imaging to age deep venous thrombosis. Ultrasound Med. Biol. **28**(6), 757–767 (2002)
21. Genet, M., Rausch, M., Lee, L., Choy, S., Zhao, X., Kassab, G., Kozerke, S., Guccione, J., Kuhl, E.: Heterogeneous growth-induced prestrain in the heart. J. Biomech. **48**(10), 2080–2089 (2015)
22. Göktepe, S., Miehe, C.: A micro–macro approach to rubber-like materials. Part III: the micro-sphere model of anisotropic mullins-type damage. J. Mech. Phys. Solids **53**(10), 2259–2283 (2005)
23. Goldhaber, S.Z., Bounameaux, H.: Pulmonary embolism and deep vein thrombosis. Lancet **379**(9828), 1835–1846 (2012)
24. Heo, S., Xu, Y.: Constructing fully symmetric cubature formulae for the sphere. Math. Comput. **70**(233), 269–279 (2001)
25. Holzapfel, G.A., Gasser, T.C., Ogden, R.W.: A new constitutive framework for arterial wall mechanics and a comparative study of material models. J. Elast. **61**(1–3), 1–48 (2000)
26. Huang, L., Nagapudi, K., Apkarian, R.P., Chaikof, E.L.: Engineered collagen-PEO nanofibers and fabrics. J. Biomater. Sci., Polym. Ed. **12**(9), 979–993 (2001)
27. Humphrey, J., Rajagopal, K.: A constrained mixture model for growth and remodeling of soft tissues. Math. Models Methods Appl. Sci. **12**(03), 407–430 (2002)
28. Jerjes-Sanchez, C.: Venous and arterial thrombosis: a continuous spectrum of the same disease? Eur. Heart J. **26**(1), 3–4 (2005)
29. Karšaj, I., Humphrey, J.D.: A mathematical model of evolving mechanical properties of intraluminal thrombus. Biorheology **46**(6), 509–527 (2009)
30. Lanir, Y., Namani, R.: Reliability of structure tensors in representing soft tissues structure. J. Mech. Behav. Biomed. Mater. **46**, 222–228 (2015)
31. Lee, Y., Naito, Y., Kurobe, H., Breuer, C., Humphrey, J.: Biaxial mechanical properties of the inferior vena cava in C57BL/6 and CB-17 SCID/bg mice. J. Biomech. **46**(13), 2277–2282 (2013)
32. Lee, Y., Lee, A., Humphrey, J., Rausch, M.: Histological and biomechanical changes in a mouse model of venous thrombus remodeling. Biorheology **52**(3), 235–245 (2015)
33. Libby, P., Theroux, P.: Pathophysiology of coronary artery disease. Circulation **111**(25), 3481–3488 (2005)
34. Lo, K., Denney, W.S., Diamond, S.L.: Stochastic modeling of blood coagulation initiation. Pathophysiol. Haemost. Thromb. **34**(2–3), 80–90 (2005)
35. Maas, S.A., Ellis, B.J., Ateshian, G.A., Weiss, J.A.: FEBio: finite elements for biomechanics. J. Biomech. Eng. **134**(1), 011005 (2012)
36. Mackman, N.: Triggers, targets and treatments for thrombosis. Nature **451**(7181), 914–918 (2008)
37. Matveyev, M.Y., Domogatsky, S.P.: Penetration of macromolecules into contracted blood clot. Biophys. J. **63**(3), 862 (1992)
38. Rausch, M.K., Humphrey, J.D.: A microstructurally inspired damage model for early venous thrombus. J. Mech. Behav. Biomed. Mater. **55**, 12–20 (2015)
39. Rausch, M.K., Kuhl, E.: On the effect of prestrain and residual stress in thin biological membranes. J. Mech. Phys. Solids **61**(9), 1955–1969 (2013)
40. Rausch, M.K., Kuhl, E.: On the mechanics of growing thin biological membranes. J. Mech. Phys. Solids **63**, 128–140 (2014)
41. Rausch, M.K., Zöllner, A.M., Genet, M., Baillargeon, B., Bothe, W., Kuhl, E.: A virtual sizing tool for mitral valve annuloplasty. Int. J. Numer. Methods Biomed. Eng. (2016). doi:10.1002/cnm.2788
42. Robbie, L., Bennett, B., Croll, A., Brown, P., Booth, N.: Proteins of the fibrinolytic system in human thrombi. Thromb. Haemost. **75**(1), 127–133 (1996)
43. Ruberti, J.W., Hallab, N.J.: Strain-controlled enzymatic cleavage of collagen in loaded matrix. Biochem. Biophys. Res. Commun. **336**(2), 483–489 (2005)
44. Sakalihasan, N., Limet, R., Defawe, O.: Abdominal aortic aneurysm. Lancet **365**(9470), 1577–1589 (2005)
45. Starling, R.C., Moazami, N., Silvestry, S.C., Ewald, G., Rogers, J.G., Milano, C.A., Rame, J.E., Acker, M.A., Blackstone, E.H., Ehrlinger, J., et al.: Unexpected abrupt increase in left ventricular assist device thrombosis. N. Engl. J. Med. **370**(1), 33–40 (2014)

46. Tepole, A.B., Kuhl, E.: Computational modeling of chemo-bio-mechanical coupling: a systems-biology approach towards wound healing. Comput. Methods Biomech. Biomed. Eng. **24**, 1–18 (2014)
47. Tong, J., Cohnert, T., Regitnig, P., Holzapfel, G.A.: Effects of age on the elastic properties of the intraluminal thrombus and the thrombus-covered wall in abdominal aortic aneurysms: biaxial extension behaviour and material modelling. Eur. J. Vasc. Endovasc. Surg. **42**(2), 207–219 (2011)
48. Tsai, T.T., Evangelista, A., Nienaber, C.A., Myrmel, T., Meinhardt, G., Cooper, J.V., Smith, D.E., Suzuki, T., Fattori, R., Llovet, A., et al.: Partial thrombosis of the false lumen in patients with acute type b aortic dissection. N. Engl. J. Med. **357**(4), 349–359 (2007)
49. Varjú, I., Sótonyi, P., Machovich, R., Szabó, L., Tenekedjiev, K., Silva, M., Longstaff, C., Kolev, K.: Hindered dissolution of fibrin formed under mechanical stress. J. Thromb. Haemost. **9**(5), 979–986 (2011)
50. Wilson, J.S., Virag, L., Di Achille, P., Karšaj, I., Humphrey, J.D.: Biochemomechanics of intraluminal thrombus in abdominal aortic aneurysms. J. Biomech. Eng. **135**(2), 021011 (2013)
51. Xu, Z., Lioi, J., Mu, J., Kamocka, M.M., Liu, X., Chen, D.Z., Rosen, E.D., Alber, M.: A multiscale model of venous thrombus formation with surface-mediated control of blood coagulation cascade. Biophys. J. **98**(9), 1723–1732 (2010)
52. Xu, Z., Kamocka, M., Alber, M., Rosen, E.D.: Computational approaches to studying thrombus development. Arterioscler. Thromb. Vasc. Biol. **31**(3), 500–505 (2011)